Transport in Porous Media (2006) 63: 399–434
DOI 10.1007/s11242-005-0108-z

Multiphase Thermohaline Convection in the Earth's Crust: I. A New Finite Element – Finite Volume Solution Technique Combined With a New Equation of State for NaCl–H_2O

SEBASTIAN GEIGER[1,*], THOMAS DRIESNER[1], CHRISTOPH A. HEINRICH[1] and STEPHAN K. MATTHÄI[2]
[1]*Department of Earth Sciences, Institute for Isotope Geology and Mineral Resources, ETH Zürich, Sonneggstr. 5, CH-8092 Zürich, Switzerland*
[2]*Department of Earth Science and Engineering, Imperial College London, SW7 2AZ, U.K.*

(Received: 22 July 2004; in final form: 7 June 2005)

Abstract. We present a new finite element – finite volume (FEFV) method combined with a realistic equation of state for NaCl–H_2O to model fluid convection driven by temperature and salinity gradients. This method can deal with the nonlinear variations in fluid properties, separation of a saline fluid into a high-density, high-salinity brine phase and low-density, low-salinity vapor phase well above the critical point of pure H_2O, and geometrically complex geological structures. Similar to the well-known implicit pressure explicit saturation formulation, this approach decouples the governing equations. We formulate a fluid pressure equation that is solved using an implicit finite element method. We derive the fluid velocities from the updated pressure field and employ them in a higher-order, mass conserving finite volume formulation to solve hyperbolic parts of the conservation laws. The parabolic parts are solved by finite element methods. This FEFV method provides for geometric flexibility and numerical efficiency. The equation of state for NaCl–H_2O is valid from 0 to 750°C, 0 to 4000 bar, and 0–100 wt.% NaCl. This allows the simulation of thermohaline convection in high-temperature and high-pressure environments, such as continental or oceanic hydrothermal systems where phase separation is common.

Key words: brine, vapor, hydrothermal, mid-ocean ridge, porphyry copper, two-phase flow, convection, numerical modeling, finite element, finite volume, NaCl–H_2O.

Nomenclature

a Property gradient [$kg\,m^{-3}\,m^{-1}$] or [$°C\ m^{-1}$].
a Dispersion coefficient [m].
A Area [m^2].
A Mass matrix [–].
c_p Isobaric heat capacity [$kJ\,kg^{-1}\ °C^{-1}$].

*Author for correspondence: e-mail: geiger@erdw.ethz.ch

$\mathcal{C}$ Courant criterion [s].
D Diffusivity [$m^2\,s^{-1}$].
e Finite element [–].
$\mathbf{D}$ Dispersion tensor [$m^2\,s^{-1}$].
g Gravity constant [$m\,s^{-2}$].
$\mathbf{g}$ Gravitational acceleration vector [$m\,s^{-2}$].
H Specific enthalpy [$kJ\,kg^{-1}$].
$\mathbf{I}$ Identity matrix [–].
k_r Relative permeability [–].
$\mathbf{k}$ Permeability tensor [m^2].
K Thermal conductivity [$W\,m^{-1}\,{}^{\circ}C^{-1}$].
$\mathbf{K}$ Stiffness matrix [–].
m Fluid mass [kg].
n Number of Lagrange points [–].
$\mathbf{n}$ Normal vector [–].
N Number of segments per finite volume [–].
$\mathcal{N}$ Vector of Lagrange points [–].
p Pressure [Pa] or [bar].
q Source/sink term [e.g., $kg\,m^{-3}\,s^{-1}$].
$\mathbf{q}$ Right-hand side vector [–].
r Radius [m].
R_{th} Thermal retardation [–].
S Saturation [–].
t Time [s].
T Temperature [°C].
$\mathbf{v}$ Velocity [$m\,s^{-1}$].
V Volume [m^3].
$\mathcal{V}$ Finite element space [–].
x Mass fraction [–].
$\mathbf{x}$ Coordinate vector [m].
X Salinity [wt% NaCl].

Greek Symbols

α Thermal expansivity [$^{\circ}C^{-1}$].
β Compressibility [Pa^{-1}].
γ Chemical expansivity [wt% $NaCl^{-1}$].
δ General diffusivity parameters [$m^2\,s^{-1}$].
Δ Increment [–].
ϵ General scalar multiplier [–].
ε Stability criterion [–].
μ Viscosity [Pa s].
ϕ Porosity [–].
Φ Finite element basis function [–].
ψ General conserved variable [e.g., $kg\,m^{-3}$].
ρ Density [$kg\,m^{-3}$].
σ Velocity divergence [s^{-1}].
Ω Computational domain [–].

Subscripts and Superscripts

crit	Property at critical point (pure H_2O).
f	Fluid (all fluid phases present).
h	Halite phase.
i	Index.
j	Index.
k	Time-step.
l	Liquid phase.
L	Longitudinal.
lat	Latent.
m	Solid matrix.
p	Pore space.
r	Rock phase.
sat	Saturation property (pure H_2O).
th	Thermal.
T	Transversal.
v	Vapor phase.
0	Ground state.

1. Introduction

The simultaneous transport of heat and solutes by aqueous fluids in porous or fractured media within the Earth's crust is a key driver for many important geological processes, such as the formation of large ore deposits, cooling of newly-formed oceanic crust along mid-ocean ridges, flow in sedimentary basins, topography-driven flow, metamorphism, or the evolution of geothermal systems. In most of these processes, the motion of fluids is dominated by buoyancy forces arising from density differences between the fluids due to pressure, temperature and compositional variations (Ingebritsen and Sanford, 1999). Convection of aqueous fluids may occur down to 9 km depth (Lüschen *et al.*, 1993; Möller *et al.*, 1997) or possibly even 15 km depth (Nesbitt and Muehlenbachs, 1991). Evidence from fluid inclusions show that crustal fluids can experience temperatures exceeding 700°C (e.g., Ulrich *et al.*, 2002).

Crustal fluids commonly contain various dissolved chemical components (Hedenquist and Lowenstern, 1994; Shmulovich *et al.*, 1995; von Damm, 1995; Barnes, 1997; Reed, 1997; Geiger *et al.*, 2002). The component that is most abundant and whose concentration can be constrained most accurately from fluid inclusion data is salt, mainly sodium chloride NaCl. We therefore consider the system NaCl–H_2O here, and the term thermohaline convection refers to the simultaneous convection of heat and NaCl by flowing fluids of variable density.

Although thermohaline convection in the Earth's crust is an important process, it has never been fully modeled for the wide range of

pressure, temperature, and salinity conditions realized in the Earth's crust. This is primarily a consequence of the decisive and challenging thermodynamic (Palliser and McKibbin, 1998a,b,c) and hydrodynamic (Phillips, 1991; Nield and Bejan, 1992) differences between the H_2O and mixed NaCl–H_2O system.

The presence of NaCl in H_2O produces a large $p-T-X$ region where a liquid and a vapor phase coexist (Figure 1). As a result, a NaCl-H_2O fluid can boil at temperatures and pressures well above the critical temperature and pressure for pure H_2O. Such two-phase fluid coexistence is frequently recorded by fluid inclusions from magmatic hydrothermal systems (Bodnar *et al.*, 1985; Heinrich *et al.*, 1999). Furthermore, crystalline salt (halite) can precipitate from the fluid at high salinities and/or low pressures, for which there is evidence from fluid inclusions in magmatic (Cloke and Kesler, 1979) and some metamorphic systems (Trommsdorff *et al.*, 1985). Numerous experimental studies have examined the phase equilibria, vapor pressures, and resulting fluid properties of NaCl–H_2O fluids (Sourirajan and Kennedy, 1962; Bischoff and Rosenbauer, 1985). These data were recently compiled into a model applicable over the entire $p-T-X$ range of crustal fluids (Palliser and McKibbin, 1998a,b,c). This published model, however, produces non-physical artifacts such as negative heat capacities in certain $p-T-X$ regions.

Convection of heat and salt is considerably different from convection of heat alone, because it can lead to double-diffusive and double-convective motion of heat and salt, i.e. flow patterns where both the advection and diffusion rates are different for the solute (NaCl) and heat (Phillips, 1991; Nield and Bejan, 1992). These processes may produce various complex and nonlinear flow instabilities even if the fluid is not boiling.

Despite these thermodynamic and hydrodynamic difficulties, fluid flow in important geologic environments has been studied numerically, making some simplifying assumptions. Most commonly it was assumed that the fluid is pure water, specifically if phase separation into a liquid and vapor phase was modeled (Hayba and Ingebritsen, 1997; O'Sullivan *et al.*, 2001). Hence, double-diffusive and double-convective effects are neglected and phase separation is restricted to temperatures and pressures below the critical point of pure H_2O. If thermohaline convection was modeled, it was often assumed that the fluid is incompressible, the Boussinesq approximation is valid, and the density depends linearly on temperature and salinity. In this case, the possibility of phase separation is a priori excluded and usually a simplified linear equation of state with constant fluid viscosities was employed (Schoofs, 1999).

Although simplifications were made in earlier studies, these provided fundamental insight into crustal fluid flow processes and solved challenging problems. For example, it could be shown why the temperatures of black

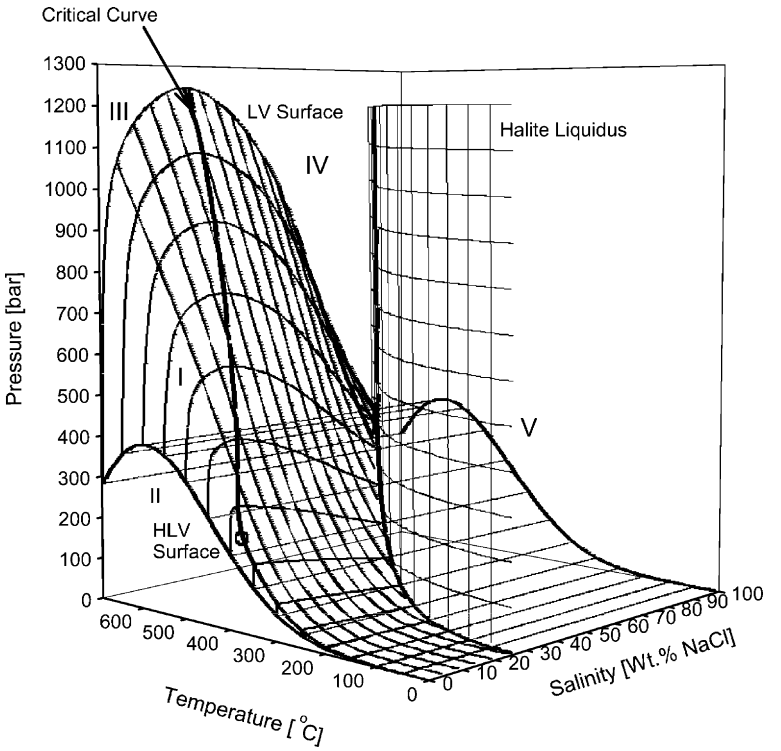

Figure 1. Phase diagram of the binary NaCl–H_2O system (Driesner and Heinrich, 2005, in revision). Five different regions can be distinguished. A region of liquid and vapor coexistence (I) bounded by the liquid plus vapor (LV) and halite plus liquid plus vapor (HLV) surfaces, a region of halite and vapor coexistence (II) bounded by the HLV surface, regions where the fluid is a single phase with either vapor-like (III) or liquid-like properties (IV) properties, and a region of halite and liquid coexistence (V) bounded by the HLV surface and the halite liquidus. The critical curve for NaCl–H_2O, which forms the crest of the LV surface, extends from the critical point of H_2O (373.976°C, 220.561 bar, open circle) to the critical point of NaCl (>3000°C, ~ 300 – 400 bar). The two-phase curve of pure H_2O starts at the triple point of pure H_2O (0.01°C, 0.0061 bar) and terminates in the critical point of pure H_2O.

smokers on the seafloor cannot exceed 400°C (Jupp and Schultz, 2000), under which conditions a magmatic pluton can be cooled most efficiently (Hayba and Ingebritsen, 1997), how various types of brine transport influence the formation of Mississippi Valley Type ore deposits (Garven *et al.*, 1999), that free thermohaline convection can drive fluid flow in sedimentary basins (Sarkar *et al.*, 1995; Schoofs *et al.*, 2000), that layered thermohaline convection may be common in geothermal systems and could explain the occurrence of distinct fluid types (Oldenburg and Pruess, 1998),

or that the interface of a brine layer and the overlying seawater at a mid-ocean ridge is not stable (Schoofs and Hansen, 2000).

Recently, several numerical studies have tried to asses the general behavior of hydrothermal systems at seawater salinity (3.2 wt.% NaCl), including the full complexity of super-critical phase separation into a low-density vapor and high-density brine phase. Seyfried *et al.* (2003) have shown, using one-dimensional simulations, that phase separation and brine condensation could account for the large chemical variability of the hydrothermal fluids expelled at the Main Endavour Field. Bai *et al.* (2003) have examined the effects of permeability and basal heat flux on one-dimensional heat-pipe solutions for multiphase hydrothermal systems at seawater salinity. Kawada *et al.* (2004) have calculated two-dimensional steady state solutions for multiphase thermohaline convection at low Rayleigh numbers and seawater salinity, using the Boussinesq approximation, constant and identical heat capacities and viscosities for both fluid phases, and neglecting the latent heat of vaporization. Lewis and Lowell (2004), assuming that heat transfer occurs mainly by thermal conduction, showed that the maximum width of the two-phase zone adjacent to an intruded dike is approximately 20 cm and halite can precipitate.

While the one-dimensional models by Seyfried *et al.* (2003) and Bai *et al.* (2003) yielded insight into the dynamics of counter-current liquid and vapor flow, they could not asses the complex multi-dimensional aspects occurring during thermohaline convection, such as oscillatory and chaotic flow patterns (Schoofs *et al.*, 1999) or transient separation of thermal and saline plumes (Oldenburg and Pruess, 1999). The study by Kawada *et al.* (2004) was the first to investigate the dynamics of multi-dimensional thermohaline convection including phase separation. Their numerical setup, however, does not represent the physics of these systems accurately. The compressibility of a liquid–vapor system is orders of magnitude higher than the compressibility of a slightly compressible liquid or highly compressible vapor (Grant and Sorey, 1979). Hence, the Boussinesq approximation cannot be applied for a liquid–vapor system. It also severely underpredicts the onset and vigor of convection if the fluid properties change nonlinearly as a function of pressure and temperature (Strauss and Schubert, 1977). In addition heat capacity and viscosity are not identical for the vapor and brine phase and vary nonlinearly over orders of magnitude as a function of pressure, temperature, and composition. Assuming that these parameters have constant and identical values for both phases is likely to lead to inaccuracies for the high-temperature systems considered by Kawada *et al.* (2004). The steady state solutions calculated by Kawada *et al.* (2004) are only applicable to low Rayleigh numbers and cannot account for the possibly high permeabilities of the continental or oceanic crust (Fisher, 1998; Manning and Ingebritsen, 1998), giving rise to instable thermohaline

convection patterns (Schoofs *et al.*, 1999). Similarly, the study by Lewis and Lowell (2004) cannot be applied to the many hydrothermal systems where convection is the dominating transport process.

Simulations of geologic processes involving both salinity variations and phase separation at elevated pressures and temperatures hence require an approach that faces two major challenges. First, a robust and consistent equation of state valid over geologically realistic pressure, temperature, and salinity ranges is necessary. Second, an accurate and numerically robust transport algorithm is required that can resolve complex geological structures in multiple dimensions and can deal with flow of two compressible, miscible fluids with contrasting properties in systems with orders of magnitude variations in permeability.

In this paper we use an accurate description of the thermodynamics of the NaCl–H_2O system (Driesner and Heinrich, 2003) in combination with a geometrically flexible, accurate, efficient, and stable transport algorithm. This tool permits us to gain new insight into the transient evolution of a variety of high-temperature, high-pressure geological processes involving the convection of NaCl–H_2O fluids. Our new transport method combines finite element with finite volume schemes. This finite element – finite volume (FEFV) method can resolve complex geological structures and many orders of magnitude of permeability variations which are widespread in the Earth's crust. It can also deal with phase separation and multiphase transport of fluid phases with greatly varying properties in double-diffusive and double-convective systems.

We first discuss the thermodynamics of the NaCl–H_2O system and the associated fluid properties. This is followed by the derivation of the governing equations for multiphase thermohaline convection. The numerical method is then described in detail. We close by discussing the implementation of the described methods into our object oriented C++ code CSP (Matthäi *et al.*, 2001).

In an accompanying paper (Geiger *et al.*, 2005), we present numerical solutions for various benchmarking tests representing sub-problems of multiphase thermohaline convection. These are compared to their reference solutions to verify the numerical method. The accompanying paper also shows the example application of phase separation of a convecting NaCl–H_2O fluid.

2. NaCl–H_2O Thermodynamics and Fluid Properties

To model convection of a NaCl–H_2O fluid, density ρ, enthalpy H, viscosity μ, and saturation S must be computed as a function of the evolving fluid pressure p, temperature T, and salinity X fields. In addition, derivatives of the basic properties ρ and H are commonly needed, i.e. the

compressibility β, thermal expansivity α, chemical expansivity γ, and isobaric heat capacity c_p. All of these fluid properties vary nonlinearly and over orders of magnitude in the NaCl–H_2O system.

2.1. PHASE DIAGRAM

The topology of the binary NaCl–H_2O system (Figure 1) is constrained by the high melting temperature of NaCl at a low vapor pressure, and by an intermediate fluid immiscibility region extending to much higher pressures. Five different regions can be distinguished in the NaCl–H_2O phase diagram (Figure 1). Region I is is a large miscibility gap in which a NaCl–H_2O fluid separates into a brine and a vapor phase. The brine phase is of higher density and has a salt concentration higher than the bulk salinity of the liquid–vapor mixture. The vapor phase is of lower density and has a salt concentration lower than the bulk salinity. To high pressures, the miscibility gap is bounded by the liquid-saturated vapor and vapor-saturated liquid surfaces. In the following, we call the combined two surfaces the liquid plus vapor (LV) surface. The crest of the LV surface is the critical curve of NaCl–H_2O. It starts at the critical point of pure H_2O (373.976°C, 220.561 bar) and extends to the critical point of pure NaCl (>3000°C, $\sim 300-400$ bar). Below the critical point of pure H_2O at $X=0$, the liquid-saturated vapor surface and vapor-saturated liquid surface meet in the saturation curve of pure H_2O. At low pressures, the miscibility gap is bounded by the halite plus liquid plus vapor (HLV) surface. Below the HLV surface at low pressures lies Region II. Here, solid salt (halite) coexists with a low-density vapor phase of near-zero salinity. Region III and IV lie above the LV surface at high pressures and temperatures. Here, the fluid has either gas-like properties and a low salinity (Region III) or liquid-like properties and a higher salinity (Region IV). A continuous transition of the fluid properties between Regions III and IV exists for pressures above and temperatures below the LV surface. If the salinity of a single-phase liquid-like fluid from Region IV is further increased, the halite liquidus is reached. In Region V, the fluid is saturated with halite, i.e. a high-density, high-salinity liquid phase coexists with halite.

A NaCl–H_2O fluid can hence take $p-T-X$ paths along which it evolves very differently from a pure H_2O fluid. For example, a fluid at 500 bar, 100°C, and 10 wt.% NaCl is isobarically heated. When the fluid encounters the LV surface, it separates into a brine and vapor phase in Region I. The fluid remains in this phase state if the temperature is increased further. The vapor fraction, however, will continue to increase. If the same fluid is isobarically heated at 300 bars, it will again separate into a brine and vapor phase in Region I when encountering the LV surface, albeit at lower temperatures. Upon further heating, the fluid will then

encounter the HLV surface. Here, the brine phase is completely boiled off, precipitating halite and proceeding into Region II. Continued heating then leads to the dissolution of halite in a newly forming brine phase when the fluid encounters the HLV surface again, just below 700°C. The fluid remains in Region I if the temperature is further increased. A pure H_2O fluid at 300 bar and 500°C, instead, is supercritical. It will remain supercritical if heated and its fluid properties change continuously from liquid to vapor like.

2.2. EXISTING FORMULATIONS

Individual $p - T - X$ regions of the NaCl–H_2O system have been intensely studied and equations of state for these regions have been derived (e.g., Rogers and Pitzer, 1982; Bischoff and Rosenbauer, 1985; Anderko and Pitzer, 1993). None of these equations of state, however, are fully suitable for the use in the present context because most formulations are valid only over limited ranges of temperature, pressure, and composition and/or provide only a small number of fluid properties. Typically, these formulations do not smoothly overlap at the boundaries of their validity ranges. This often produces discontinuities in the fluid properties which precludes the combination of different formulations for different portions of the phase diagram (Figure 1). In addition, the more modern equations of state (Anderko and Pitzer, 1993) are free energy formulations. Therefore, these equations do not provide the fluid properties as a function of the most practical state variables of the fluid flow simulation, i.e. p, T, and X. For example, direct extraction of the compositions of coexisting liquid and vapor phases is hence not possible. Instead, costly iterative schemes are required to generate this basic information.

An alternative approach is the derivation of correlation functions for the fluid properties of interest. This general approach was recently used by (Palliser and McKibbin, 1998a,b,c), employing different correlation formulae above and below the critical temperature of water for vapor pressures, densities, and enthalpies on the LV surface and in the one-phase regions. Unfortunately, their mathematical formalism, which employs a function for sub-critical and a function for supercritical temperatures for each fluid property, yields non-physical artifacts where the two functions meet. For example, the enthalpy versus temperature curve for a given composition shows a negative slope just above the critical temperature of water, implying a negative heat capacity. Also, some linear interpolation schemes in the one phase regions provide properties that can be substantially different from known experimental data, in particular in the highly compressible region around and above the critical point of water. This region, however, is frequently encountered in the simulation of magmatic hydrothermal systems.

We therefore decided to develop our own set of correlations (Driesner and Heinrich, 2003, 2005; Driesner, 2005). The formulation is based on a critical review of essentially all published experimental data on the phase boundaries in the NaCl–H_2O system and all available data for volumetric and thermodynamic properties. Its accuracy is within the uncertainty of the best available experimental data, resolving most of the apparent inconsistencies. Its validity range is from 0 to 1000°C, from 0 to 5000 bar, and from 0 to 100 wt.% NaCl. The pure water side is described by the functions of Haar *et al.* (1984) since this is available in a convenient form for computation (Bauer, 2002). For this study, we have used an older version (Driesner and Heinrich, 2003) of the model by Driesner and Heinrich (2005) and Driesner (2005), which is only valid from 0 to approximately 750°C, 0 to 4000 bar, and 0–100 wt.% NaCl.

2.3. FLUID PROPERTIES AND PHASE STATE

The correlations are based on temperature, pressure, and salinity. For any given $p-T-X$ combination, the phase state of the fluid along with the properties ρ, H, μ, S, β, and c_p can be calculated directly for each individual phase. Pressure-temperature profiles of fluid density ρ_f and enthalpy H_f at varying salinities are shown in Figure 2. ρ_f and H_f change continuously in Region IV. Both properties change rapidly from liquid-like to vapor-like along the interface between Regions IV and I because the vapor fraction increases rapidly with increasing temperature or decreasing pressure in Region I. Due to the presence of halite in Region II, a discontinuity in ρ_f and H_f appears at the boundaries between Region II and Regions IV and I.

2.4. FLUID PROPERTIES AT TWO-PHASE CONDITIONS

Our formulation for the NaCl–H_2O system provides the properties for each individual phase. Special care must be taken when computing the saturation S, compressibility β, thermal expansivity α, and chemical expansivity γ at two-phase conditions, because they are a function of the proportions of the two phases present. At two-phase conditions, β, α, and γ describe the thermodynamic behavior of the brine-vapor mixture.

2.4.1. *Saturation*

In Region I (Figure 1), the saturations of the phases are computed employing a balance for the mass fraction NaCl in the liquid and vapor phase

$$S_l = \frac{\rho_v\,(X_v - X)}{\rho_l\,(X - X_l) + \rho_v\,(X_v - X)} \quad \text{and} \quad S_v = 1 - S_l. \tag{1}$$

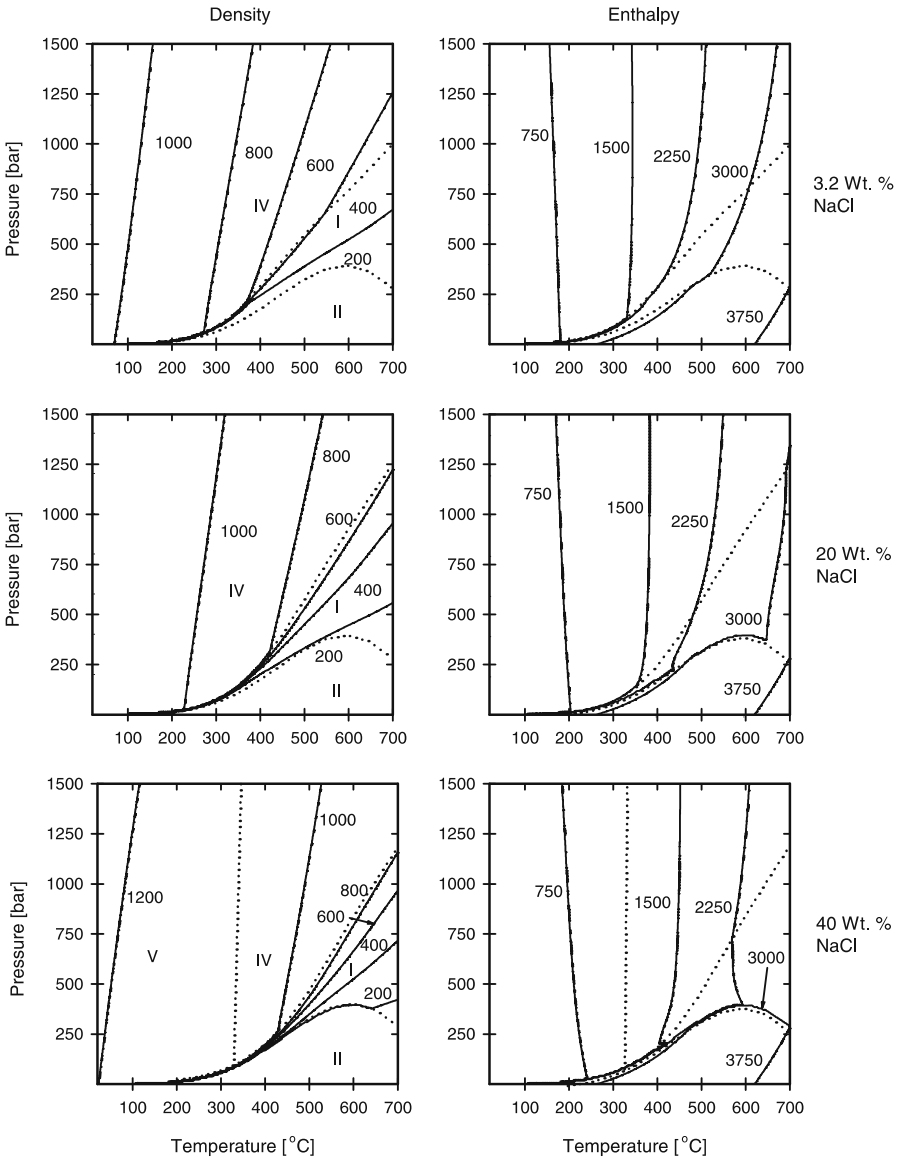

Figure 2. $p-T$ profiles of fluid density $\rho_f = (\rho_v S_v + \rho_l S_l)$ (left) and enthalpy $H_f = (H_v \rho_v S_v + H_l \rho_l S_l)/(\rho_v S_v + \rho_l S_l)$ (right) at bulk salinities of 3.2, 20, and 40 wt.% NaCl (top to bottom). Units of the contour labels are in [kg m^{-3}], respectively [kJ kg^{-1}]. The roman numbers in the density profiles indicate the phase regions from Figure 1. Dotted lines mark boundaries between different phase regions. Note that the salinity of the fluid phase is below 40 wt.% NaCl in Region V where halite coexists with a liquid phase and practically zero in Region II where halite coexists with a vapor phase.

In Region II or V, halite precipitates and its saturation S_h is computed as

$$S_h = \begin{cases} \dfrac{\rho_v (X_v - X)}{\rho_h (X - X_h) + \rho_v (X_v - X)} & \text{in Region II,} \\ \dfrac{\rho_l (X_l - X)}{\rho_h (X - X_h) + \rho_l (X_l - X)} & \text{in Region V.} \end{cases} \tag{2}$$

Since part of the pore volume is now occupied by solid salt, the saturation of the fluid phase that coexists with halite remains one. Halite is treated as rock matrix. This changes the porosity of the medium

$$\phi = \phi_0 (1 - S_h), \tag{3}$$

where ϕ_0 is the initial porosity and a potential hysteresis effect is ignored here. Depending on the nature of the porous medium, a corresponding change in the permeability $\mathbf{k}$ can be computed using an empirical ϕ-$\mathbf{k}$ relation. In Region II the amount of precipitated halite is very small. Hence S_h is initially low. Thus changes in porosity are of importance for the hydrodynamics only if halite precipitates for a long time in Region II or coexists with a liquid phase in Region V.

2.4.2. *Compressibility*

The isothermal compressibility β is defined as

$$\beta = \frac{1}{\rho} \left(\frac{\mathrm{d}\rho}{\mathrm{d}p} \right)_{T,X} = -\frac{1}{V} \left(\frac{\mathrm{d}V}{\mathrm{d}p} \right)_{T,X}, \tag{4}$$

where V is the specific volume of fluid. This formula is applied directly at single-phase conditions. At two-phase conditions in Region I, however, a pressure drop will cause liquid to evaporate and a pressure increase will force vapor to condense. This is accompanied by a redistribution of mass and heat. As a result, the two-phase compressibilities $\widetilde{\beta}$ are orders of magnitude higher than those for single-phases. We approximate these as (Grant and Sorey, 1979)

$$\widetilde{\beta} = \frac{1}{\phi} \left[(1 - \phi) \rho_r c_{pr} + \phi S_l \rho_l c_{pl} \right] \left[\frac{\rho_l - \rho_v}{(h_v - h_l) \rho_l \rho_v} \right]^2 (T + 273.15). \tag{5}$$

2.4.3. *Thermal Expansivity*

The thermal expansivity α is defined as

$$\alpha = -\frac{1}{\rho} \left(\frac{\mathrm{d}\rho}{\mathrm{d}T} \right)_{p,X} = \frac{1}{V} \left(\frac{\mathrm{d}V}{\mathrm{d}T} \right)_{p,X} \tag{6}$$

and can be computed directly using this formula at single phase conditions. dT is zero in Region I if the fluid continues to boil or condense at constant pressure. α hence becomes infinity if computed from Equation (6). Computing the mass of fluid that has boiled off from Equation (26), the volume change during boiling ΔV, i.e. the two-phase thermal expansivity $\widetilde{\alpha}$, is given by

$$\widetilde{\alpha} = \Delta V = m_f x_l \left(\frac{1}{\rho_v} - \frac{1}{\rho_l} \right), \tag{7}$$

where m_f is the total mass of fluid. Similarly, the mass fraction of condensed vapor x_v and the volume change due to condensation can be computed.

2.4.4. *Chemical Expansivity*

The chemical expansivity γ is defined as

$$\gamma = \frac{1}{\rho} \left(\frac{d\rho}{dX} \right)_{p,T} = -\frac{1}{V} \left(\frac{dV}{dX} \right)_{p,T} \tag{8}$$

and can be computed directly from this formula at single phase conditions but requires special treatment at two-phase conditions. In Region I, the chemical expansivity $\widetilde{\gamma}$ is given by

$$\widetilde{\gamma} = \left(\frac{1}{\rho_l} - \frac{1}{\rho_v} \right) \frac{1}{X_l - X_v}. \tag{9}$$

3. Governing Equations

We formulate the governing transport equations in terms of fluid pressure p, temperature T, and salinity X. We assume that porous medium and fluids are always in thermodynamic equilibrium, heat conduction is predominant in the rock and can be described by a bulk thermal conductivity, and that capillary pressure effects are negligible (Bear, 1972; Faust and Mercer, 1979a; Huyakorn and Pinder, 1983). For simplicity, we omit any fluid, energy, or salt source terms in the discussion of the governing equations.

3.1. FLUID MASS CONSERVATION

The mass balance of a fluid consisting of two fluid phases can be expressed as (Bear, 1972)

$$\phi \frac{\partial \rho_f}{\partial t} + \rho_f \frac{\partial \phi}{\partial t} = -\nabla \cdot (\mathbf{v}_v \rho_v) - \nabla \cdot (\mathbf{v}_l \rho_l), \tag{10}$$

where ϕ is the porosity of the porous medium, ρ is the density, $\mathbf{v}$ is the Darcy velocity vector of the fluid phase, and the subscripts l and v denote the liquid and vapor phase, respectively. The average fluid density ρ_f is given by

$$\rho_f = S_l \rho_l + S_v \rho_v, \tag{11}$$

where S is the saturation (volume fraction) and requires $S_l + S_v = 1$. The fluid velocity $\mathbf{v}_i$ for each fluid phase i is derived from Darcy's law (Bear, 1972)

$$\mathbf{v}_i = -\mathbf{k} \frac{k_{ri}}{\mu_i} [\nabla p - \rho_i \mathbf{g}]. \tag{12}$$

Here $\mathbf{k}$ is the permeability tensor, k_r is the relative permeability, μ is the fluid viscosity, p is the fluid pressure, and $\mathbf{g} = [0, 0, -g]^T$ is the vector of gravitational acceleration. The total velocity of the fluid $\mathbf{v}_f$ is the sum of both phase velocities $\mathbf{v}_f = \mathbf{v}_l + \mathbf{v}_v$. A common theoretical function for the simultaneous flow of a liquid and vapor phase is (Faust and Mercer, 1979b)

$$k_{rl} = S_l^4 \quad k_{rv} = S_v^2 \left(1 - S_l^2\right). \tag{13}$$

Xu (2004) has shown that in situations where diffusive transport becomes important (e.g., at low permeabilities or very steep concentration gradients in NaCl), diffusion terms for both NaCl and H_2O should be added to Equation (10).

The fluid density ρ_f is a function of p, T, and X. This is expressed as

$$\begin{aligned} d\rho_f &= \left(\frac{\partial \rho_f}{\partial p}\right)_{T,X} \mathrm{d}p + \left(\frac{\partial \rho_f}{\partial T}\right)_{p,X} \mathrm{d}T + \left(\frac{\partial \rho_f}{\partial X}\right)_{T,p} \mathrm{d}X \\ &= \rho_f \left(\beta_f \mathrm{d}p - \alpha_f \mathrm{d}T + \gamma_f \mathrm{d}X\right), \end{aligned} \tag{14}$$

where β_f is the fluid's compressibility, α_f is the fluid's thermal expansivity, and γ_f is the fluid's chemical expansivity as defined above.

The change in porosity ϕ in Equation (10) is not only due to precipitation of halite (Equation 3), but also partly a function of the compressibility of the pore space

$$\frac{\partial \phi}{\partial t} = \frac{\partial \phi}{\partial p} \frac{\partial p}{\partial t}. \tag{15}$$

This relation, however, does not account for the compressibility of the solid rock matrix. The compressibility of the rock β_r, i.e. solid plus pore space, is given by (Bear, 1972)

$$\beta_r = -(1 - \phi) \frac{1}{V_m} \frac{\mathrm{d}V_m}{\mathrm{d}p} - \phi \frac{1}{V_p} \frac{\mathrm{d}V_p}{\mathrm{d}p}, \tag{16}$$

where V is the volume and the subscripts m and p denote the solid matrix and pore space, respectively. In the hot hydrothermal systems considered

here, the fluid compressibility is commonly orders of magnitude larger than the rock compressibility, i.e. $\beta_f \gg \beta_r$.

A parabolic equation that describes the evolution of fluid pressure p results from inserting Equation (12) into (10) and using Equations (14) and (16) to account for the compressibility of the fluid, solid matrix, and pore space

$$\begin{aligned}\rho_f \left(\beta_r + \phi\beta_f\right) \frac{\partial p}{\partial t} \\ = \nabla \cdot \left[\mathbf{k}\left(\frac{k_{rl}}{\mu_l}\rho_l + \frac{k_{rv}}{\mu_v}\rho_v\right)\nabla p\right] + \\ + \mathbf{k}\left(\frac{k_{rl}}{\mu_l}\rho_l^2 + \frac{k_{rv}}{\mu_v}\rho_v^2\right) g\nabla z + \phi\rho_f\left(\gamma_f \frac{\partial X}{\partial t} - \alpha_f \frac{\partial T}{\partial t}\right).\end{aligned} \tag{17}$$

Equation (17) expresses the fluid mass conservation in the systems in terms of changes in fluid pressure. Note that the thermal expansivity of the fluid α_f can readily be expanded to include the thermal expansion of the rock as well.

3.2. SOLUTE MASS CONSERVATION

Conservation of the mass fraction NaCl in H_2O is given by (Bai *et al.*, 2003)

$$\begin{aligned}\phi \frac{\partial}{\partial t}\rho_f X_f = -\nabla \cdot (\mathbf{v}_v \rho_v X_v) - \nabla \cdot (\mathbf{v}_l \rho_l X_l) + \\ + \nabla \cdot (\mathbf{D}_l \nabla \rho_l X_l) + \nabla \cdot (\mathbf{D}_v \nabla \rho_v X_v),\end{aligned} \tag{18}$$

where $\rho_f X_f$ is the total mass of NaCl in the fluid defined as

$$\rho_f X_f = S_l \rho_l X_l + S_v \rho_v X_v. \tag{19}$$

The dispersivity tensor $\mathbf{D}_i$ of phase i is given by

$$\mathbf{D}_i = D_{pi}\mathbf{I} + (a_L - a_T)\frac{\mathbf{v}_{ix}\mathbf{v}_{iz}}{|\mathbf{v}_i|} + a_T |\mathbf{v}_i| \mathbf{I}, \tag{20}$$

where D_{pi} is the porous-medium diffusivity of NaCl in phase i, a_L and a_T are the longitudinal and transversal dispersivities, respectively, and $\mathbf{I}$ is the identity matrix.

3.3. ENERGY CONSERVATION

Conservation of energy by the fluid phases is given by (Bear, 1972; Delaney, 1982)

$$\left((1-\phi)\,\rho_r c_{pr} + \phi\left(S_l \rho_l c_{pl} + S_v \rho_v c_{pv}\right)\right)\frac{\partial T}{\partial t} = -\nabla\cdot\left(\mathbf{v}_v c_{pv}\rho_v T\right) - \nabla\cdot\left(\mathbf{v}_l c_{pl}\rho_l T\right) + \nabla\cdot\left(K\nabla T\right), \tag{21}$$

where c_p is the isobaric heat capacity and K is the thermal bulk conductivity of fluid and rock commonly given by (Bear, 1972)

$$K = (1-\phi)K_r + \phi K_f. \tag{22}$$

The subscript r denotes the rock property. It should be pointed out that formulations for K are available in the literature that use a different weighting of K_r and K_f, for example $K = K_f^{\phi} + K_r^{(1-\phi)}$ (Raffensperger, 1996). K can also be replaced, analogous to Equation (18), by a thermal dispersion tensor. In Equation (20), D_{pi} then corresponds to K and a to the thermal dispersivity that is scaled by the heat capacity c_p and fluid density ρ (Marsiliy, 1986).

From Equation (21) it can be shown that the temperature front moves at the heat transfer velocity $\mathbf{v}_{th}$ defined as

$$\mathbf{v}_{th} = \frac{c_{pl}\rho_l \mathbf{v}_l + c_{pv}\rho_v \mathbf{v}_v}{\phi\left(S_l c_{pl}\rho_l + S_v c_{pv}\rho_v\right) + (1-\phi)\,c_{pr}\rho_r}. \tag{23}$$

From Equation (18) it can be seen that the salt front moves at the pore velocity

$$\mathbf{v}_p = \frac{\mathbf{v}_l + \mathbf{v}_v}{\phi}. \tag{24}$$

Hence, the thermal front is retarded with respect to the salt front by the factor R_{th}

$$R_{th} = \frac{\mathbf{v}_{th}}{\mathbf{v}_p} < 1 \tag{25}$$

3.3.1. *Latent Heat during Boiling*

By writing the left-hand side of Equation (21) in terms of $c_p \partial T/\partial t$, the latent heat of vaporization that is intrinsically used in an enthalpy-based formulation (e.g., Faust and Mercer, 1979a), is no longer accounted for. Using pure H_2O as an example, this can be compensated in the following manner.

To avoid artificial flash boiling (all liquid boils to vapor during a single time-step), an energy balance is employed if $T^t > T_{\text{sat}}$ and $T^{t-\Delta t} < T_{\text{sat}}$ to compute the mass fraction of the liquid phase Δx_l that boils off. T_{sat} is

the saturation temperature for the given pressure. Assuming that ϕ is small such that the energy in the solid phase is higher than in the fluid phase, i.e. the rock matrix buffers the energy provided by the fluid, the mass fraction of the liquid phase Δx_l being boiled off is given by

$$\Delta x_l = \frac{(1-\phi)\,\rho_r c_{pr}\left(T^t - T_{\text{sat}}\right)}{H_{\text{lat}}\phi\rho_{\text{l,sat}} S_{\text{l,sat}}}, \tag{26}$$

where H_{lat} is the latent heat of boiling $H_{\text{lat}} = H_v - H_l$. The saturation of the liquid phase is then computed as

$$S_l = 1 - \left(\frac{(1-\Delta x_l)\, m_l/\rho_l}{\Delta x_l m_l/\rho_v + (1-\Delta x_l)\, m_l/\rho_l}\right)_{\text{sat}} \tag{27}$$

For the case of condensation ($T^t < T_{\text{sat}}$ and $T^{t-\Delta t} > T_{\text{sat}}$), the energy balance yielding the mass fraction vapor being condensed Δx_v is given by

$$\Delta x_v = \frac{(1-\phi)\,\rho_r c_{pr}\left(T_{\text{sat}} - T^t\right)}{H_{\text{lat}}\phi\rho_{v,\text{sat}} S_{v,\text{sat}}}. \tag{28}$$

The saturation of the vapor phase can be calculated from

$$S_v = \left(\frac{(1-\Delta x_v)\, m_v/\rho_v}{\Delta x_v m_v/\rho_l + (1-\Delta x_v)\, m_v/\rho_v}\right)_{\text{sat}}. \tag{29}$$

4. Numerical Methods

4.1. EXISTING NUMERICAL APPROACHES

The governing equations are strongly nonlinear and coupled, because the fluid properties ρ, c_p, μ, α, β, γ, and the saturation S depend nonlinearly on p, T, and X and may vary over orders of magnitude. The governing equations have mixed parabolic (diffusive) and hyperbolic (advective) character.

The numerical techniques commonly employed in research codes to solve the governing equations are finite difference (FD) (Hayba and Ingebritsen, 1994), integrated finite difference (IFD) (Pruess, 1987, 1991), or finite element methods (FE) (Zyvoloski *et al.*, 1996). These techniques are formulated such that they solve simultaneously for pressure, temperature, and concentration, i.e. the solution approach is fully coupled. A Newton iteration is employed to account for the nonlinearities. Each method is, in principal, well suited to solve the governing equations for multiphase flow, heat and/or salt transport and the computer codes have been successfully applied to simulate challenging physical problems.

The comprehensive discussion by Steefel and MacQuarrie (1996) has highlighted the advantages and disadvantages of each numerical technique. FD methods are a common choice because they are relatively easy to implement and grid generation is straightforward. The drawback is that such uniform FD grids may not resolve geological structures adequately. IFD methods allow a more flexible grid generation and better representation of the geologic domain (Narasimhan and Witherspoon, 1976). Since gradients are still calculated on the basis of FD schemes, IFD grids require that the interface between two nodes is perpendicular to the line connecting them. This requirement may cause problems when generating grids that need to resolve geometrically complex structures or when dealing with tensor quantities. FE methods can efficiently resolve complex non-rectangular structures, for example if Delaunay grids are employed in two (Shewchuk, 2002) or poly-element meshes in three dimensions (Matthäi, 2003; Matthäi *et al.*, 2004b). Of these three numerical methods, the FE technique is probably the most difficult to implement in computer codes and special software is needed to generate quality meshes, particularly in three dimensions. All methods have in common that, unless special care is taken, non-physical oscillations in the vicinity of concentration or temperature fronts may occur if the characteristic time for advection greatly exceeds that for diffusion. Upstream weighting techniques can be employed to alleviate this problem, but this introduces numerical dispersion, i.e., concentration or temperature fronts are artificially broadened. Numerical dispersion can be limited by high-resolution spatial schemes, for example total variation diminishing (TVD) schemes (Harten, 1983; Sweby, 1984). Such a scheme has been successfully employed in combination with the IFD method in the computer code TOUGH (Oldenburg and Pruess, 2000). Upstream weighting in FE methods imposes certain requirements onto the finite element mesh, reducing its ability to resolve complex geological structures. If these requirements are not met, conditions can occur in which the transmissibility becomes negative, i.e. fluid will flow from low to high potential (Forsyth, 1991).

Aside from these advantages and disadvantages of each method to resolve geological structures and deal with advection-dominated transport, the fully coupled solution approach has additional drawbacks. The linearized global solution matrices are often very poorly conditioned such that small time-steps are required, the use of fast matrix solvers (e.g., algebraic multigrid solvers) may be prohibited, and convergence towards a unique solution is not guaranteed (Trangenstein and Bell, 1989a,b; Burri, 2004). A fully coupled implicit formulation commonly requires as many iteration-steps as a decoupled explicit formulation needs grid-restricted time-steps (Küther, 2002; Burri, 2004). This combination of relatively small time-steps with a large number of iterations decreases computational

efficiency of fully coupled implicit schemes (Huber and Helmig, 1999; Burri, 2004).

4.2. COMBINATION OF FINITE ELEMENTS AND FINITE VOLUMES

Recently, the combination of higher-order FEFV schemes was suggested to be a very efficient approach that overcomes the aforementioned numerical problems of modeling the non-linear flow of two immiscible and incompressible fluid phases in porous and fractured media (Trangenstein and Bell, 1989a,b; Durlofsky, 1993; Huber and Helming, 1999; Geiger *et al.*, 2004). In the FEFV method, the pressure equation is solved decoupled from the conservation equations. This decoupling is based on the well-known implicit pressure explicit saturation (IMPES) approach for modeling immiscible and incompressible two-phase flow (Aziz and Settari, 1979). In the IMPES method it is permissible to solve the governing equations separately because they operate on different timescales: Pressure diffuses more rapidly to steady state than saturation changes advect through the porous medium. This decoupling of pressure and conservation equations, however, permits to employ the optimal numerical method for the solution of the respective sub-equations: Finite volume methods model the hyperbolic and finite element methods the parabolic equations (Durlofsky, 1993; Huber and Helmig, 1999; Geiger *et al.*, 2004). It was further shown that FEFV methods can be successfully applied to model nonlinear two-phase flow in highly heterogeneous and geometrically complex porous medium (Huber and Helmig, 1999; Geiger *et al.*, 2004) or compressible and compositional multiphase flow (Dicks, 1993; Bergamaschi *et al.*, 1998).

In order to derive a robust solution algorithm that makes use of the advantages that the finite element and finite volume methods have to offer for solving certain types of equations, we linearize the governing equation by decoupling the pressure equation from the energy and solute conservation equations. In this operator-splitting, the hyperbolic sub-equations are solved by the finite volume method by surface-integration of the flux term over an area A, e.g.

$$\int_A \mathbf{n} \cdot \left[\mathbf{k} \frac{k_{ri}}{\mu_i} \nabla p \right] \mathrm{dA}, \tag{30}$$

where $\mathbf{n}$ is the outward-pointing normal of A. The parabolic sub-equations are solved by the finite element method by volume integration of the flux term over a volume V, e.g.

$$\int_V \left[\nabla \mathbf{k} \frac{k_{ri}}{\mu_i} \nabla p \right] \mathrm{d}V. \tag{31}$$

The operator splitting of the governing equations is done as follows (Strang, 1968). Consider a general advection diffusion equation for a conserved quantity ψ of the form

$$\epsilon \frac{\partial \psi}{\partial t} = \nabla \cdot (\delta \nabla \psi) - \nabla \cdot (\mathbf{v}\psi) + q, \tag{32}$$

where δ is the diffusivity parameter, ϵ is some multiplier (e.g., porosity), and q is a source or sink of ψ. The partial solution $\hat{\psi}^{t+\Delta t}$ of Equation (32) for the diffusion part $\nabla \cdot (\delta \nabla \psi)$ at time $t + \Delta t$ is obtained by finite element methods by solving

$$\epsilon \frac{\hat{\psi}^{t+\Delta t} - \psi^t}{\Delta t} = \nabla \cdot \left(\delta \nabla \psi^t\right) + q. \tag{33}$$

The result of the diffusive contribution $\hat{\psi}^{t+\Delta t}$ is then used to solve the advection part $-\nabla \cdot (\mathbf{v}\psi)$ of Equation (32) to obtain the final solution $\psi^{t+\Delta t}$ at time $t + \Delta t$ by using a finite volume method on

$$\epsilon \frac{\psi^{t+\Delta t} - \hat{\psi}^{t+\Delta t}}{\Delta t} = -\nabla \cdot \left(\mathbf{v}\hat{\psi}^{t+\Delta t}\right). \tag{34}$$

Comparable to the IMPES method (Aziz and Settari, 1979), this operator-splitting approach results in a parabolic pressure-diffusion equation (Equation 17), which describes mass conservation of the fluid phases, and conservation equations for energy (Equation (21)) and salt (Equation (18)). As shown by Kissling *et al.* (1992) and Young (1993), pressure diffusion is faster than the advection of saturation in typical geothermal reservoirs and two-phase geothermal flows are hence asymptotically identical to the Buckley–Leverett theory for immiscible and incompressible two-phase flow, which is commonly modeled by IMPES-based numerical schemes (Durlofsky, 1993; Huber and Helmig, 1999; Geiger *et al.*, 2004).

Hence, as in the IMPES approach, we solve the governing equations for pressure, temperature, and salinity sequentially. First, the fluid pressure is updated and the fluid velocities are obtained from Darcy's law (Equation (12)). Then the energy and solute conservation equations are solved. Last, the fluid properties are updated from the equation of state using the new values for p, T, and X. The volume change of the fluid due to temperature and concentration changes feeds back as source terms into the solution of the fluid pressure equation for the next time-step. The decoupling of the governing equations into a pressure evolution, and transport equations for energy and solute in conjunction with implicit and explicitly time-stepping offers considerable advantages:

– Each sub-equation is solved by the best suited numerical method.
– Node-centered finite volumes are constructed on the basis of the finite elements and are fully mass conserving even for strongly heterogeneous permeability fields and complex geometric structures.
– Spatially higher-order accurate transport methods are employed to resolve the hyperbolic shock-fronts.
– Due to the parabolic nature of the fluid pressure equation, a change in the mobility $\mathbf{k}\, k_{ri}/\mu_i$ of phase i at a single finite element forces the fluid pressure to change in the entire model. This is implemented using a very robust implicit temporal discretization.
– The global solution matrices for the governing equations are symmetric positive definite, well conditioned and, hence, suitable for fast algebraic multigrid solvers.
– Iterative methods that may require very small time-steps or fail to converge are no longer necessary.

4.3. SPATIAL DISCRETIZATION

We discretize two-dimensional domains by a constrained conforming Delauney triangulation (Shewchuk, 2002). This allows to resolve complex structures in great detail. Node-centered finite volumes are constructed on the basis of the finite elements, such that a dual finite volume grid is formed (Figure 3). It is not necessary to restrict the finite element mesh to triangles in two dimensions or tetrahedra in three dimensions. Node-centered finite volumes can be constructed also for mixed element meshes consisting of different finite element types, which allows to maximize geometric flexibility while minimizing the number of nodes and elements, specifically in three dimensions (Matthäi, 2003; Matthäi *et al.*, 2004b).

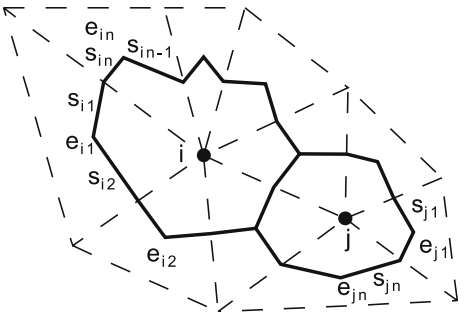

Figure 3. Node-centered finite volumes (bold lines) on nodes i and j constructed on a triangular finite element mesh consisting of triangles e (dashed lines). The barycenters of the finite elements e are connected with the midpoints of their edges to form finite volume segments s.

4.4. FINITE ELEMENT FORMULATION

We solve the fluid pressure equation (Equation (17)) and the parabolic components of the energy (Equation (21)) and salt (Equation (18)) conservation equations by the Bubnov–Galerkin formalism. While mixed-element formulations are often used to simultaneously compute fluid pressure and velocity (Huber and Helmig, 1999), the lowest order mixed-element method requires to solve between 1.5 and 4 times more unknowns than a Galerkin formulation but yields exactly the irreducible Galerkin formulation (Cordes and Kinzelbach, 1996). Thus, excellent results can be obtained using a Galerkin formulation to solve Equation (17) even for nonlinear flow systems (Geiger *et al.*, 2004; Matthäi and Belayneh, 2004). As the Galerkin finite element formulation is well known and excellent descriptions can be found (Huyakorn and Pinder, 1983; Zienkiewicz and Taylor, 2000), only a brief description is given here. We discuss the Galerkin discretization for the parabolic part (Equation (33)) of the general advection-diffusion equation (Equation (32)). By appropriate substitution of ψ, δ, ϵ, and q, Equations (17), (21), and (18) are solved.

The computational domain Ω is discretized into a set of finite elements spanning the finite element space $\mathcal{V}$ of continuous linear polynomial functions. $\mathcal{V}$ has n Lagrange points $\mathcal{N} = \{\mathbf{x}_i\}_{i=1}^n$ and a set of basis functions $\{\Phi_i(\mathbf{x})\}_{i=1}^n$. Here, $\mathbf{x}$ is the coordinate vector in two or three dimensions. By writing $\psi \in \mathcal{V}$ as $\psi(\mathbf{x}) = \sum_{j=1}^n \psi(\mathbf{x}_j)\Phi_j(\mathbf{x})$, the basis functions Φ can be used to approximate Equation (33) for a fixed time t as

$$\int_\Omega \epsilon \frac{\partial \psi}{\partial t} \Phi_i \, \mathrm{d}\mathbf{x} = \int_\Omega \delta \nabla \psi \nabla \Phi_i \, \mathrm{d}\mathbf{x} + \int_\Omega q \Phi_i \, \mathrm{d}\mathbf{x}. \tag{35}$$

With the decomposition $\psi(\mathbf{x}, t) = \sum_{j=1}^n \psi_j(t)\Phi_j(\mathbf{x})$, the coupled system of ordinary differential equations is defined as

$$\sum_{j=1}^n \frac{\mathrm{d}\psi_j}{dt}(t)\mathbf{A}_{ij}(t) = \sum_{j=1}^n \psi_j(t)\mathbf{K}_{ij}(t) + q_i(t), \tag{36}$$

where the mass matrix $\mathbf{A}$, stiffness matrix $\mathbf{K}$, and on the right-hand side vector $\mathbf{q}$ are given by

$$\begin{aligned} \mathbf{A}_{ij}(t) &= \int_\Omega \epsilon \Phi_j \Phi_i \, \mathrm{d}\mathbf{x}, \\ \mathbf{K}_{ij}(t) &= \int_\Omega \nabla \Phi_j \delta \nabla \Phi_i \, \mathrm{d}\mathbf{x}, \\ \mathbf{q}_i(t) &= \int_\Omega q \Phi_i \, \mathrm{d}\mathbf{x}. \end{aligned} \tag{37}$$

Note that we diagonalize $\mathbf{A}$ for each finite element by mass-lumping using a row-sum technique (Geiger *et al.*, 2004).

An implicit Euler time-stepping formulation is used to evolve the solution of ψ from time t to time $t+\Delta t$ as

$$\sum_{j=1}^{n}(\mathbf{A}_{ij}^{t+\Delta t}+\Delta t\mathbf{K}_{ij}^{t+\Delta t})\hat{\psi}_j^{t+\Delta t}=\sum_{j=1}^{n}\mathbf{A}_{ij}^{t}\psi_j^{t}+\Delta t\mathbf{q}_i^{t+\Delta t}. \tag{38}$$

This time-discretization ensures that the solution is unconditionally stable as long as the matrices are positive definite and that no iterative methods need to be used if $\mathbf{A}$ or $\mathbf{K}$ are functions of ψ (Zienkiewicz and Taylor, 2000).

From the updated pressure field, element-wise constant fluid velocities are obtained by differentiating the pressure field and solving for Darcy's law (Equation (12)) within each finite element. Although the fluid velocities are discontinuous between adjacent finite elements, they are continuous across the face of a node-centered finite volume and conserve mass on the finite volumes (Durlofsky, 1994).

4.5. FINITE VOLUME FORMULATION

The fluid velocity field computed from Equation (12) is integrated over the node-centered finite volumes. Integrating Equation (34) over the finite volume V_i connected to node i yields

$$\int_{V_i}\epsilon_i\frac{\partial\psi}{\partial t}\,\mathrm{d}V_i=-\int_{V_i}\nabla\cdot(\mathbf{v}\psi)\,\mathrm{d}V_i \tag{39}$$

Application of the divergence theorem to Equation (39) and discretizing in time using an explicit Euler method leads to the solution that evolves the diffusion step $\hat{\psi}^{t+\Delta t}$ to the final solution $\psi^{t+\Delta t}$

$$\psi_i^{t+\Delta t}=\hat{\psi}_i^{t+\Delta t}-\frac{\Delta t}{\epsilon_i\,|V_i|}\sum_{j}^{N_i}\left[A_j\mathbf{v}_j^t\hat{\psi}_{j*}^{t+\Delta t}\right]\cdot\mathbf{n}_j, \tag{40}$$

where A_j is the area, respectively length in two dimensions, of the finite volume segment j. $|V_i|$ is the volume, respectively area in two-dimensions, of control volume i. $\mathbf{n}_j$ is the outward-pointing normal of segment j. N_i is the total number of segments belonging to finite volume i. The subscript $j*$ denotes that the value of ψ is taken from the upwind finite volume at segment j. We reconstruct the gradient $\mathbf{a}$ of ψ in i using a least squares method and the MINMOD limiter to avoid spurious oscillations and ascertain that the scheme is total variation diminishing as discussed in Geiger *et al.* (2004). This yields a second order accurate solution of Equation (34) in space and resolves shock-fronts occurring in purely hyperbolic systems

in great detail while maintaining mass conservation for nonlinear systems (Geiger *et al.*, 2004).

Although the finite volume discretization is straightforward, care must be taken when applying Equation (40) to the hyperbolic parts of the energy (Equation (21)) and salt conservation (Equation (18)) laws. Using the definition of $\mathbf{v}_{\text{th}}$ in Equation (23) and noting that $\nabla \cdot (\mathbf{v}_{\text{th}} T) = \mathbf{v}_{\text{th}} \cdot \nabla T + T \nabla \cdot \mathbf{v}_{\text{th}}$, the divergence, σ, of $\mathbf{v}_{\text{th}}$ is non-zero, i.e.

$$\sigma = \nabla \cdot \mathbf{v}_{\text{th}} \neq 0 \tag{41}$$

the hyperbolic part of the energy conservation law written in terms of $\mathbf{v}_{\text{th}}$ takes the form

$$\frac{\partial T}{\partial t} = -\mathbf{v}_{\text{th}} \cdot \nabla T - T \nabla \cdot \mathbf{v}_{\text{th}}. \tag{42}$$

This hyperbolic part of the energy conservation law is discretized as

$$T_i^{t+\Delta t} = \hat{T}_i^{t+\Delta t} - \frac{\Delta t}{|V_i|} \sum_j^{N_i} \left[A_j \mathbf{v}_{thj}^t \hat{T}_{j*}^{t+\Delta t} \right] \cdot \mathbf{n}_j + \frac{\Delta t}{|V_i|} \sigma_i \hat{T}_i^{t+\Delta t}. \tag{43}$$

For the hyperbolic parts of the salt conservation equation (Equation 18), the finite volume algorithm for each phase i is defined as

$$\rho_i^{t+\Delta t} X_i^{t+\Delta t} = \hat{\rho}_i^{t+\Delta t} \hat{X}_i^{t+\Delta t} - \frac{\Delta t}{|V_i|} \sum_j^{N_i} \left[A_j \mathbf{v}_{ij}^t \hat{\rho}_{ij*}^{t+\Delta t} \hat{X}_{ij*}^{t+\Delta t} \right] \cdot \mathbf{n}_j. \tag{44}$$

4.5.1. *Error Estimation*

We conserve energy in our scheme using a $c_p - T$ formulation (Equation (21)) employing the heat transfer velocity $\mathbf{v}_{th}$ (Equation (23)) to express energy changes as a variation in temperature T advected at $\mathbf{v}_{\text{th}}$. This is, strictly speaking, not an energy conservation scheme because temperature is conserved instead of enthalpy H. This scheme implicitly assumes that c_p is constant over a single time-step. This can introduce an error if temperature changes rapidly over a single time-step due to advection and enthalpy varies non-linearly within the given temperature interval. In this case, a fluid enthalpy change ΔH cannot be accurately represented by the linear approximation $\Delta H \approx c_p \Delta T = (\mathrm{d}H/\mathrm{d}T)\, \Delta T$. As a consequence, fluid temperature T at the new time-step is over- or under-estimated by a factor ΔT^* (Figure 4). The largest errors occur along the critical isobar (220.0561 bar in the formulation of Haar *et al.* (1984)) of pure H_2O. Here, enthalpy changes rapidly with temperature, specifically close to the critical point where $c_p \to \infty$. The temperatures, however, do not become infinite for infinite fluid heat capacities because energy transport is buffered by the

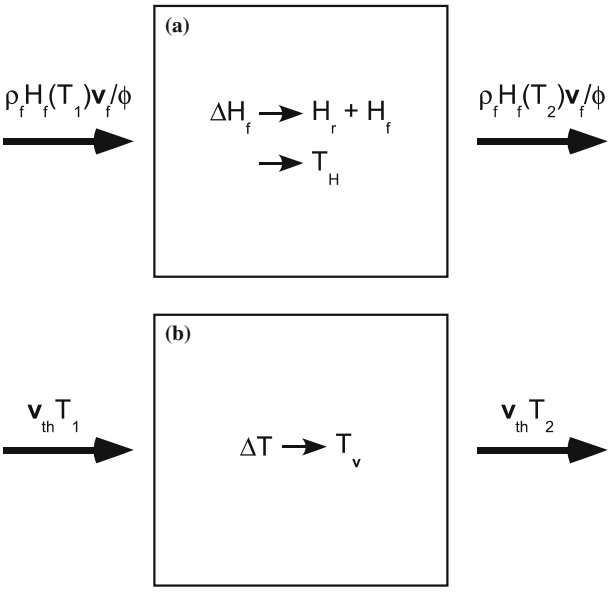

Figure 4. Error source for a $\mathbf{v}_{\text{th}}$-based energy transport scheme. Fluid advects energy and mass, expressed as enthalpy H_f and density ρ_f, at pore velocity $\mathbf{v}_f/\phi$ in and out of a control volume (a). The entering fluid is hotter than the exiting fluid ($T_1 > T_2$). Hence fluid enthalpy increases with ΔH_f. After thermal equilibration between fluid H_f and rock enthalpy H_r, they are at temperature T_H and $T_1 \geqslant T_H > T_2$. In our $\mathbf{v}_{\text{th}}$-based energy advection scheme, this process is approximated by transport of temperature T in and out of a control volume at velocity $\mathbf{v}_{\text{th}}$ (b). Since $T_1 > T_2$, this results in a temperature $T_{\mathbf{v}}$ and $T_1 \geqslant T_{\mathbf{v}} > T_2$. Due to the definition of $\mathbf{v}_{\text{th}}$ (Equation 23), rock and fluid are in equilibrium at $T_{\mathbf{v}}$. The two temperatures are not equal, i.e. $T_{\mathbf{v}} \neq T_h$, if enthalpy H_f changes rapidly over increment ΔT because $\Delta H \neq c_p \Delta T$. For the estimation of error ΔT^* between T_H and $T_{\mathbf{v}}$ (Figure 5), it is assumed that $\mathbf{v} = 1.0$. All other properties are calculate as a function of temperature and porosity ϕ with $\Delta T = T_1 - T_2 = T_{\text{crit}} - T_2$

rock matrix. A calculation of ΔT^* at the critical isobar for various ΔT and porosity values shows that this error only becomes significant if ΔT is unrealistically high (Figure 5). Since we use an explicit time-stepping scheme to solve advection equations, the time-step and, hence, ΔT is small if $\mathbf{v}_{\text{th}}$ is large. Temperature variations during a single time-step are therefore commonly $\Delta T \ll 10^{\circ}\text{C}$. The error hence remains small over this temperature increment, i.e. $\Delta T^* \sim -1.5\%$. Away from the critical point, ΔT^* is lower, i.e. $|\Delta T^*| < 0.01\%$, even for unrealistically large ΔT variations during a single time-step. T_{crit} is the critical temperature of pure H_2O.

4.6. TIME STEPPING

The pressure equation (Equation (17)) is solved by an implicit Euler time-discretization and the time-step Δt could hence be chosen to be arbitrary

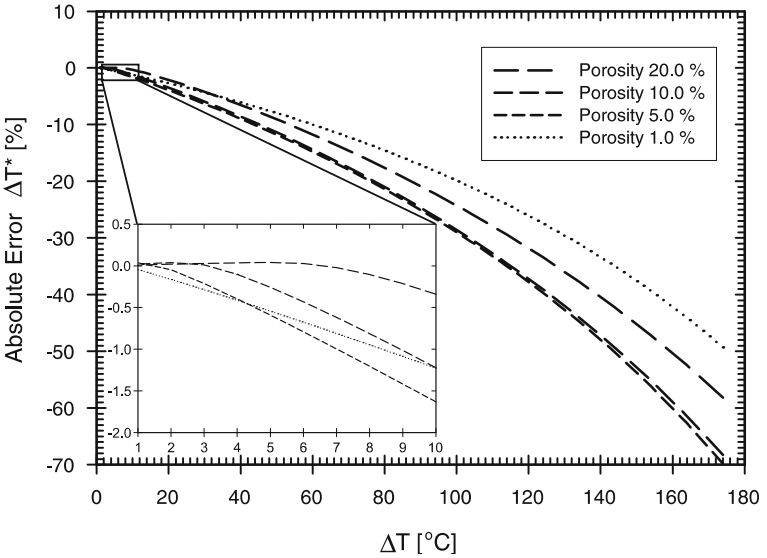

Figure 5. Absolute error $\Delta T^* = (T_H - T_v)/T_H$ along the critical isobar of pure H_2O resulting from the $\mathbf{v}_{\text{th}}$-based energy advection scheme (Figure 4).

large. The size of Δt, however, is controlled by the Courant Friedrich Levy (CFL) criterion computed for the explicit Euler solution of the hyperbolic parts of the energy and solute conservation equations (Equations (21) and (18)). The CFL criterion $\mathcal{C}_{\text{th}}$ for energy conservation equation is given by

$$\mathcal{C}_{\text{th}} = \left(\frac{r_i}{\mathbf{v}_{\text{th}}^{\max}} \right)_{\min} \qquad i \in \mathcal{V}. \tag{45}$$

The CFL criterion $\mathcal{C}_x$ and for the solute conservation equation

$$\mathcal{C}_x = \left(\frac{r_i}{\mathbf{v}_p^{\max}} \right)_{\min} \qquad i \in \mathcal{V}. \tag{46}$$

Here r_i is the approximate radius of the control volume i. The superscript max denotes the maximum elemental velocity within an element e_i belonging to control volume i (Figure 3). Note that by using r_i rather than the diameter of the finite volume cell, the CFL criterion is reduced by a factor 2. Since $R_{\text{th}} \leqslant 1$ and $\phi \leqslant 1$, the two CFL criteria are not equal and usually $\mathcal{C}_{\text{th}} \gg \mathcal{C}_x$. Hence it is convenient to set the time-step Δt equal to $\mathcal{C}_{\text{th}}$. This, however, violates the stability criterion for the hyperbolic parts of Equation (18) because $\mathcal{C}_{\text{th}} \gg \mathcal{C}_x$. They can be solved using a smaller sub-time-step Δt^* that is equal to $\mathcal{C}_x$. When $\sum \Delta t^* = \Delta t$, the hyperbolic parts of equation (18) are solved for exactly the same time-step as all other equations, albeit using $\mathcal{C}_{\text{th}}/\mathcal{C}_x$ calculations. This sub-time-stepping

saves computational costs because it allows for a relaxation of Δt for all governing equations but the hyperbolic parts of Equation (18). At the same time, however, it grants that the CFL criterion for the each transport equation is not violated. This is permissible for

$$\Delta t = \begin{cases} \mathcal{C}_{th} & \text{if } \frac{\mathcal{C}_x}{\mathcal{C}_{th}} \leqslant \varepsilon_1 \quad \text{and} \quad \frac{\Delta X \gamma_f}{\Delta T \alpha_f} \leqslant \varepsilon_2, \\ \mathcal{C}_x \frac{1}{\max(\varepsilon_1, \varepsilon_2)} & \text{otherwise.} \end{cases} \tag{47}$$

where ε is a user defined tolerance. As long as the thermal front moves slower than the salt front by a given factor and density variations due to concentration changes are smaller than those due to temperature changes by a given factor, the global time-step can be set equal with the CFL criterion for the energy transport equation.

We introduce an additional stability criterion for the global time-step to avoid instabilities if the CFL criterion increases significantly between two successive time-steps $k-1$ and k

$$\Delta t = \begin{cases} \mathcal{C}^k & \text{if } \frac{\mathcal{C}^k - \mathcal{C}^{k-1}}{\mathcal{C}^k} \leqslant \varepsilon_3, \\ \mathcal{C}^k + \left(\mathcal{C}^k - \mathcal{C}^{k-1}\right) \varepsilon_3 & \text{otherwise.} \end{cases} \tag{48}$$

4.7. SEQUENTIAL SOLUTION

The sequential solution of the governing equations uses a linearization of the equation of state (Dicks, 1993). The fluid velocities from the previous time-step are employed to evolve the hyperbolic system of Equations (21) and (18) using the explicit finite volume method freezing the pressure in time and computing the advection of T and X for $t + \Delta t$. The size of Δt is given by Equations (47) and (48) using the phase velocities from the previous time-step. The diffusive terms of the energy and salt conservation laws (Equations (21) and (18)) are updated using the implicit finite element method (Figure 6). The compressibility β, mobilities $\rho_i k_{ri}/\mu_i$, expansivities α and γ are updated after the transport step. Finally, the pressure equation (Equation (17)) is solved for time $t + \Delta t$ via the finite element method for the updated parameters. The updated pressure field yields the phase velocities at $t + \Delta t$ for the next transport step.

4.8. SPLITTING ERROR

The splitting of the governing equations into pressure and transport equations introduces an error of the order $\mathcal{O}(\Delta t)$ for the pressure fields that can be reduced using iterative techniques (Dicks, 1993). Mass conservation, however, is not affected by this error. It also has been shown that the splitting error is relatively small even for compressible multiphase simulations

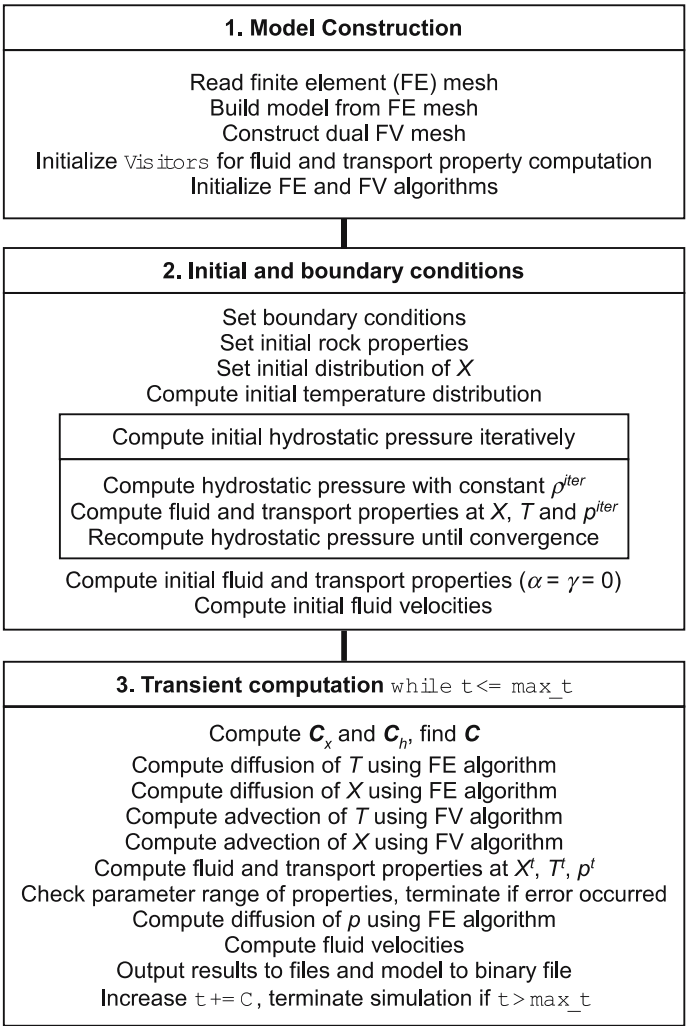

Figure 6. Flow chart of the solution procedure for multiphase thermohaline convection simulations in CSP.

and that it only results in a slight dislocation of the saturation fronts. While iteration can reduce the error in the pressure field, the corrected field may become non-physical if phase changes occur (Dicks, 1993). For highly compressible fluids, the reduction of the CFL criterion by a factor of 2, the use of a first order accurate finite volume algorithm when phase changes occur introduces enough numerical dissipation for the results to be stable and oscillation-free (Dicks, 1993). Since our CFL criterion is computed on the radii of the finite volume cell it automatically introduces the required reduction factor of 2. Our finite volume scheme is also automatically first order accurate when phase changes occur.

4.8.1. *Second Order Accuracy in Time*

The splitting error introduced by the decoupling of the governing equations can be reduced from first to second order accuracy by using a predictor-corrector time-stepping scheme. In this improved Euler time-discretization, the transport equations for energy and salt (Equations (21) and (18)) are solved for a half-step in the predictor step. The dependent variables, i.e. $\mu, \rho, k_r, \alpha, \beta$, and γ are then evaluated at time $t + \Delta t/2$ such that, after solving the pressure equation (Equation (17)) at time $t + \Delta t/2$, the fluid velocities $\mathbf{v}$ can be obtained at time $t + \Delta t/2$. These fluid velocities are then employed in the corrector step to evolve Equations (21) and (18) from time t to $t + \Delta t$ with the flux given at time $t + \Delta t/2$. Finally, Equation (17) is evolved from time t to $t + \Delta t$.

5. Implementation

Our new formalism to model multiphase thermohaline convection has been implemented in the object-oriented C++ library 'Complex System Platform' (CSP) (Matthäi *et al.*, 2001). CSP is used extensively for high-resolution multi-physics simulations in two and three-dimensions such as immiscible two-phase flow in reservoirs with complex geological structures (Burri, 2004; Geiger *et al.*, 2004; Matthäi *et al.*, 2004b; Belayneh *et al.*, 2005), reactive solute transport (Geiger *et al.*, 2002; Matthäi, 2003), heat and solute transport in hydrothermal systems (Matthäi *et al.*, 2004a), or fluid flow in geometrically realistic fracture networks (Matthäi and Roberts, 1996; Matthäi *et al.*, 1998; Matthäi and Belayneh, 2004). The advantage of the object-oriented design is the modularity, reusability, and extensibility of the code that is impossible to obtain when programming in procedural languages. Reusability and extensibility, however, is crucial when simulating such processes as multiphase thermohaline convection because they comprise a series of component-processes that must be computed by individual modules.

CSP employs the state-of-the-art algebraic multigrid solver SAMG (Stueben, 2002) to solve the system of algebraic equations that arise from the finite element and finite volume discretization. Fluid and transport properties are updated using the Visitor pattern (Gamma, 2002) on the finite element – finite volume hierarchy. Visitor objects automatically check input and output properties for validity when interacting with each other. They raise exceptions when computations fail. A 105 MB binary lookup table calculated from the implementation of the pure H_2O equation of state (Haar *et al.*, 1984) in the C-library PROST (Bauer, 2002) provides the properties for pure H_2O from 5 °C to 800°C and 1–4000 bars. The equation of state for NaCl–H_2O extracts the properties of pure H_2O from the lookup table using bi-linear interpolation with 1°C and 2.5 bar spacing, or

0.1°C and 0.1 bar spacing near the critical point. Figure 6 depicts a flow chart of the implementation and solution algorithm in CSP.

6. Conclusions

A new computational formulation for the simulation of transient multiphase thermohaline convection is presented. A novel equation of state is employed for the thermodynamic properties of the NaCl–H_2O system from 0 to 750°C, 0 to 4000 bar, and 0 to 100 wt.% NaCl. The governing equations are decoupled into a parabolic pressure diffusion equation and hyperbolic and parabolic parts of the energy and salt conservation equations. The pressure diffusion equation is evolved in time using an implicit finite element algorithm. The hyperbolic parts of the conservation equations are solved by an explicit second order accurate finite volume method employing fluid velocities derived from Darcy's law and the updated pressure field. The parabolic components of the energy and salt conservation equations are also solved by an implicit finite element method. Our formulation satisfies the conservation laws without the necessity of costly nonlinear iteration methods.

The novel solution algorithm allows the modelling of thermohaline convection and fluid flow in a variety of geological settings where $p - T - X$ conditions are such that boiling occurs, for example in continental magmatic hydrothermal systems or mid-oceanic hydrothermal systems, and which were insufficiently modeled by single-phase thermohaline convection or pure H_2O fluid flow. In a companion paper (Geiger *et al.*, 2005), the benchmarking of the algorithm is discussed and an example application is presented.

Acknowledgements

We thank Steve Roberts, Patrick Jenny, Adrian Burri, and Dim Coumou for helpful discussions. The thoughtful and constructive comments by three anonymous reviewers have significantly improved the quality of this manuscript. Funding was provided by the Swiss National Science Foundation, grants SNF-20-59544.99 and 20002-100735/1.

Appendix A. Volume Derivatives at Two-Phase Conditions

A.1. THERMAL EXPANSIVITY

The fluid volume at two-phase conditions V can be calculated as

$$V = m_f \left(\frac{x_l}{\rho_l} + \frac{x_v}{\rho_v} \right) \tag{A.1}$$

Noting that $x_l = (x - x_v)/(x_l - x_v)$ and $x_v = 1 - x_l$, Equation (A.1) can be written as

$$V = m_f \left(\frac{(x - x_v)/(x_l - x_v)}{\rho_l} + \frac{(1 - x - x_v)/(x_l - x_v)}{\rho_v} \right) \tag{A.2}$$

The mass fraction of the liquid phase x_l that is being boiled is given in Equation (26), the mass fraction of the vapor phase x_v that condenses in Equation (28). The change in mass of the two phases is simply $\Delta m_l = m_f x_l$ and $\Delta m_v = m_f x_v$, respectively. The change in volume ΔV_f during boiling due to a temperature change corresponds to the thermal expansivity. It can now be straightforwardly calculated from the above equations as

$$\Delta V_f = \tilde{\alpha} = \Delta m_v \left(\frac{1}{\rho_v} - \frac{1}{\rho_l} \right) \tag{A.3}$$

A.2. CHEMICAL EXPANSIVITY

The derivative of the two-phase fluid volume V (Equation A.1) with respect to salinity, $\partial V / \partial X$ is

$$\frac{\partial}{\partial X} \left[\frac{X - X_v}{X_l - X_v} \left(\frac{1}{\rho_l} - \frac{1}{\rho_v} \right) + \frac{1}{\rho_v} \right]. \tag{A.4}$$

Applying the chain-rule yields

$$\left(\frac{1}{\rho_l} - \frac{1}{\rho_v} \right) \frac{d}{\mathrm{d}X} \frac{X - X_v}{X_l - X_v} + \frac{X - X_v}{X_l - X_v} \frac{d}{\mathrm{d}X} \left(\frac{1}{\rho_l} - \frac{1}{\rho_v} \right) + \frac{d}{\mathrm{d}X} \frac{1}{\rho_v} \tag{A.5}$$

Noting that the density derivatives are zero allows further simplification and provides the chemical expansivity at two-phase conditions $\tilde{\gamma}$

$$\tilde{\gamma} = \left(\frac{1}{\rho_l} - \frac{1}{\rho_v} \right) \frac{1}{X_l - X_v} \tag{A.6}$$

References

Anderko, A. and Pitzer, K. S.: 1993, Equation-of-state representation of phase equilibria and volumetric properties of the system NaCl–H_2O above 573 K, *Geochim. Cosmochim. Acta* **57**, 1657–1680.

Aziz, K. and Settari, A.: 1979, *Petroleum Reservoir Simulation*, Applied Science Publishers, Barking.

Bai, W., Xu, W. and Lowell, R. P.: 2003, The dynamics of submarine geothermal heat pipes, *Geophys. Res. Lett.* **30**, 110.

Barnes, H. L.: 1997, *Geochemistry of Hydrothermal Ore Deposits, 3rd edn*, John Wiley, New York.

Bauer, O.: 2002, *PROST 4.1, PROperties of Water and STeam.* http://www.tt.tu-harburg.de/mitarbeiter/Ehemalige/engel/PROST/PROST.h tml, Technische Universität Hamburg–Harburg, Germany.

Bear, J.: 1972, *Dynamics of Fluids in Porous Media*, Dover, New York.
Belayneh, M., Matthäi, S. K. and Geiger, S.: Numerical simulation of viscous immiscible displacement in layered fractured limestone reservoir analogues. *AAPG Bulletin*, in press.
Bergamschi, L., Mantica, S. and Manzini, G.: 1998, A mixed finite element-finite volume formulation of the Black-Oil model, *SIAM J. Sci. Comput.* **20**, 970–997.
Bischoff J. L. and Rosenbauer, R. J.: 1985, An empirical equation of state for hydrothermal seawater (3.2 Percent NaCl). *Amer. J. Sci.* **285**, 725–763.
Bodnar, R. J., Burnham, C. W. and Sterner. S. M.: 1985, Synthetic fluid inclusions in natural quartz. III. Determination of phase equilibrium properties in the system H_2O–NaCl to 1000°C and 1500 bars. *Geochim. Cosmochim. Acta*, **49**, 1861–1873.
Burri, A.: 2004, Implementation of a multiphase flow simulator using a fully upwind galerkin method within the CSP multiphysics toolkit, Unpublished Diploma Thesis, Eidgenössische Technische Hochschule Zürich, Switzerland.
Cloke, P. L. and Kesler, S. E.: 1979, Halite trend in hydrothermal solutions, *Econ. Geol.* **74**, 1823–1831.
Cordes, C. and Kinzelbach, W.: 1996, Comment on "Application of the mixed hybrid finite element approximation in a groundwater flow model: Luxury or necessity?", R. Mosé, P. Siegel, P. Ackerer, and G. Chavent (eds.), *Water Resour. Res.* **32**, 1905–1909.
de Marsiliy, G: 1986, *Quantitative Hydrogeology,* Academic Press, New York.
Delaney, P. T.: 1982, Rapid intrusion of magma into wet rock: Groundwater flow due to pore pressure increases. *J. Geophys. Res.* **87**, 7739–7756.
Dicks, E. M.: 1993, Higher order Godounov black-oil simulations for compressible flow in porous media, PhD thesis, University of Reading, U.K.
Driesner, T. and Heinrich, C. A.: 2003, Accurate P-T-X-V-H correlations for the system NaCl–H_2O from 0 to 800 °C, 0 to 500 Mpa, and 0 to 1 X_{NaCl}, *Acta Mineralog. Petrograph. Abstr. Ser.* **2**, 55–56.
Driesner, T. and Heinrich, C. A.: 2005, The system NaCl–H_2O. I. Correlation formulae for phase relations in temperature-pressure-composition space from 0 to 1000°C, 0 to 5000 bar, and 0 to 1 X_{NaCl}, *Geochim. Cosmochim. Acta,* in revision.
Driesner, T.: The system NaCl–H_2O. II. Molar volume, enthalpy, and isobaric heat capacity from 0 to 1000°C, 0 to 5000 bar, and 0 to 1 X_{NaCl} *Geochim. Cosmochim. Acta*, in revision.
Durlofsky, L. J.: 1993, A triangle based mixed finite-element finite-volume technique for modeling two phase flow through porous media, *J. Comput. Phys.* **105**, 252–266.
Durlofsky, L. J.: 1994, Accuracy of mixed and control volume finite element approximations to Darcy velocity and related quantities, *Water Resour. Res.* **30**, 965–973.
Faust, C. R. and Mercer, J. W.: 1979a, Geothermal reservoir simulation 1. Mathematical models for liquid- and vapor-dominated hydrothermal systems, *Water Resour. Res.* **15**, 23–30.
Faust, C. R. and Mercer, J. W.: 1979b, Geothermal reservoir simulation 2. Numerical solution techniques for liquid- and vapor-dominated hydrothermal systems, *Water Resour. Res.* **15**, 31–46.
Fisher, A.T.: 1998, Permeability within basaltic oceanic crust, *Rev. Geophysics* **36**, 143–182.
Forsyth, P. A.: 1991, A control volume finite element approach to NAPL groundwater contamination, *SIAM J. Sci. Comput.* **12**, 1029–1057.
Gamma, E.: 2002, *Design patterns: Elements of Reusable Object Oriented Software*, Addison-Wesley, Reading, MA.
Garven, G., Appold, M. S., Toptygina, V. I. and Hazlett, T. J.: 1999, Hydrogeologic modeling of the genesis of carbonate-hosted lead-zinc ores, *Hydrogeol. J.* **7**, 108–126.

Geiger, S., Haggerty, R., Dilles, J. H., Reed, M. H. and Matthäi, S. K.: 2002, New insights from reactive transport modelling: the formation of the sericitic vein envelopes during early hydrothermal alteration at Butte, Montana, *Geofluids* **2**, 185–201.

Geiger, S., Roberts, S., Matthäi, S. K., Zoppou, C. and Burri, A.: 2004, Combining Finite element and finite volume methods for efficient multiphase flow simulations in highly heterogeneous and structurally complex geologic media, *Geofluids* **4**, 284–299.

Geiger, S., Driesner, T., Heinrich, C. A. and Matthäi, S. K.: 2006, Multiphase thermohaline convection in the Earth's crust: II. Benchmarking and application of a finite element – finite volume solution technique with a NaCl–H_2O equation of state, *Transport Porous Media*, **63**, 417–443.

Grant, M. A. and Sorey, M. L.: 1979, The compressibility and hydraulic diffusivity of a water-steam flow, *Water Resour. Res.* **15**, 684–686.

Haar, L., Gallagher, J. S. and Kell, G. S.: 1984, *NBS/NRC Steam Tables*, Hemisphere Publishing Corporation, Washingdon, DC.

Harten, A.: 1983, High resolution schemes for hyperbolic conservation laws, *J. Comput. Phys.* **49**, 357–393.

Hayba, D. O. and Ingebritsen, S. E.: 1994, *The Computer Model HYDROTHERM, A Three-Dimensional Finite-Difference Model to Simulate Ground-Water Flow and Heat Transport in the Temperature Range of 0 to 1200°C*. U.S. Geological Survey Water-Resources Investigations Report 94–4045.

Hayba, D. O. and Ingebritsen, S. E.: 1997, Multiphase groundwater flow near cooling plutons, *J. Geophys. Res.* **102**, 12235–12252.

Hedenquist, J. W. and Lowenstern, J. B.: 1994, The role of magmas in the formation of hydrothermal ore-deposits. *Nature* **370**, 519–527.

Heinrich, C. A., Günther, D., Audétat, A., Ulrich, T. and Frischknecht, R.: 1999, Metal fractionation between magmatic brine and vapor, determined by microanalysis of fluid inclusions, *Geology* **27**, 755-758.

Huber, R. and Helmig, R.: 1999, Multi-phase flow in heterogeneous porous media: A classical finite element method versus and implicit pressure-explicit saturation-based mixed finite element-finite volume approach, *Int. J. Numer. Meth. Fluids* **29**, 899–920.

Huyakorn, P. S. and Pinder, G. F.: 1983, *Computational Methods in Subsurface Flow*, Academic Press, New York.

Ingebritsen, S. E. and Sanford, W. E.: 1999, *Groundwater in Geologic Processes*, Cambridge University Press, Cambridge.

Jupp, T. and Schultz, A.: 2000, A thermodynamic explanation for black smoker temperatures, *Nature* **403**, 880–883.

Kawada, Y., Yoshida, S. and Watanabe, S.: 2004, Numerical simulations of mid-ocean ridge hydrothermal circulation including the phase separation of seawater, *Earth Planets Space* **56**, 193–215.

Kissling W., McGuinness, M., McNabb, A., Weir, G., White, S. and Young, R.: 1992, Analysis of one-dimensional horizontal two-phase flow in geothermal reservoirs, *Transport Porous Media* **7**, 223–253.

Küther, M.: 2002, Error estimates for numerical approximations to scalar conservation laws. PhD thesis, Universität Freiburg, Germany.

Lewis, K. C. and Lowell, R P.: 2004, Mathematical modeling of phase separation of seawater near an igneous dike, *Geofluids* **4**, 197–209.

Lüschen, E., Sobolev, S., Werner, U., Söller, W. *et al.*: 1993, Fluid reservoir (questionable) beneath the KTB drillbit indicated by seismic shear-wave observations, *Geophys. Res. Lett.* **20**, 923–926.

Manning, C. E. and Ingebritsen, S. E.: 1998, Permeability of the continental crust: Implications of geothermal data and metamorphic systems, *Rev. in Geophys.* **37**, 127–150.
Marsiliy, G. de: 1986, *Quantative Hydrogeology* Academic press, New York.
Matthäi, S. K. and Roberts, S.: 1996, The influence of fault permeability on single-phase fluid flow near fault-sand intersections: Results from steady-state high-resolution models of pressure-driven fluid flow, *AAPG Bulletin* **80**, 1763–1779.
Matthäi, S. K., Aydin, A., Pollard, D. D. and Roberts, S.: 1998, Numerical simulation of departures from radial drawdown in a faulted sandstone reservoir with joints and deformation bands, in: G. Jones, Q. J. Fisher, and R. J. Knipe, (eds), *Faulting, Fault Sealing and Fluid Flow in Hydrocarbon Reservoirs*, *Geological Society London, Special Publications* **147**, 157–191.
Matthäi, S. K., Geiger, S. and Roberts, S.: 2001, *Complex Systems Platform: CSP3D3.0: User's Guide*. http://e-collection.ethbib.ethz.ch/show?type=4bericht&nr=239, Eidgenössische Technische Hochschule Zürich, Switzerland.
Matthäi, S. K.: 2003, Fluid flow and (reactive) transport in fractured and faulted rock, *J. Geochem. Exploration* **78-79**, 179–182.
Matthäi, S. K., Heinrich, C. A. and Driesner, T.: 2004a, Is the Mount Isa copper deposit the product of forced brine convection in the footwall of a major reverse fault? *Geology* **32**, 357–360.
Matthäi, S. K., Mezentsev, A. and Belayneh, M.: 2004b, Control-volume finite-element two-phase experiments with fractured rock represented by unstructured 3D hybdrid meshes, *SPE Paper presented at the SPE Reservoir Simulation Symposium Houston, Texas, U.S.A*, SPE93341.
Matthäi, S.K. and Belayneh, M.: 2004c, Fluid flow partitioning between fractures and a permeable rock matrix, *Geophys. Res. Lett.* **31**, L07602.
Möller, P., Weise, S. M., Althaus, E., Bach *et al.* W.: 1997, Paleofluids and recent fluids in the upper continental crust: Results from the German Continental Deep Drilling Program (KTB), *J. Geophys. Res.* **102**, 18233–18254.
Narasimhan, T. N. and Witherspoon, P. A.: 1976, An integrated finite difference method for analyzing fluid flow in porous media, *Water Resour. Res.* **12**, 57–64.
Nesbitt, B. E. and Muehlenbachs, K.: 1991, Stable isotopic constraints on the nature of the syntectonic fluid regime in the Canadian Cordillera, *Geophys. Res. Lett.* **18**, 963–966.
Nield, D. A. and Bejan, A.: 1992, *Convection in Porous Media*, Springer-Verlag, Berlin.
Oldenburg, C. and Pruess, K.: 1998, Layered thermohaline convection in hypersaline geothermal systems, *Transport Porous Media* **33**, 29–63.
Oldenburg, C. and Pruess, K.: 1999, Plume separation by transient thermohaline convection in porous media, *Geophys. Res. Lett.* **26**, 2997–3000.
Oldenburg, C. and Pruess, K.: 2000, Simulation of propagating fronts in geothermal reservoirs with the implicit Leonard total variation diminishing scheme, *Geothermics* **29**, 1–25.
O'Sullivan, M. J., Pruess, K., and Lippman, M. J.: 2001, State of the art of geothermal reservoir simulation, *Geothermics* **30**, 395–429.
Palliser, C. and McKibbin, R.: 1998a, A model for deep geothermal brines, I: T-p-X state-space description, *Transport Porous Media* **33**, 65–80.
Palliser, C. and McKibbin, R.: 1998b, A model for deep geothermal brines, II: Thermodynamic properties – density, *Transport Porous Media* **33**, 129–154.
Palliser, C. and McKibbin, R.: 1998c, A model for deep geothermal brines, III: Thermodynamic properties – enthalpy and viscosity, *Transport Porous Media* **33**, 155–171.
Phillips, O. M.: 1991, *Flow and Reactions in Permeable Rocks,* Cambridge University Press, Cambridge.

Pruess, K.: 1987, *TOUGH User's Guide*, U.S. Nuclear Regulatory Commission, Report NUREG/CR-4645.

Pruess, K.: 1991, *TOUGH2 – A General Purpose Numerical Simulator for Multiphase Fluid and Heat Flow*, Lawrence Berkeley Laboratory Report, LBL–29400.

Raffensperger, J. P.: 1996, Numerical simulation of sedimentary basin-scale hydrochemical processes, in: M. Y. Corapcioglu, (ed.), *Advances in Porous Media* **3**, 185–305.

Reed, M. H.: 1997, Hydrothermal alteration and its relation to ore fluid composition, in H. L. Barnes, *Geochemistry of Hydrothermal Ore Deposits, 3rd edn*, 303–365.

Rogers P. S. Z. and Pitzer, K. S.: 1982, Volumetric properties of aqueous sodium chloride solutions, *J. Phys. Chem. Refer. Data* **11**, 15–81.

Sarkar, A., Nunn, J. A. and Hanor, J. S.: 1995, Free thermohaline convection beneath allochtonous salt sheets – An agent for salt dissolution and fluid flow in Gulf-Coast sediments, *J. Geophys. Res.* **100**, 18085–18092.

Schoofs, S.: 1999, Thermochemical convection in porous media. An application to hydrothermal systems and magmatic intrusions, *Geologica Ultraiectina*, 179.

Schoofs, S., Spera, F. J. and Hansen, U.: 1999, Chaotic thermohaline convection in low-porosity hydrothermal systems, *Earth and Planetary Sci. Lett.* **174**, 213–229.

Schoofs, S., Trompert, R. A. and Hansen, U.: 2000, Thermochemcial convection in and beneath intracratonic basins: Onset and effects. *J. Geophys. Res.* **105**, 25567–25585.

Schoofs, S. and Hansen, U.: 2000, Depletion of a brine layer at the base of the ridge-crest hydrothermal system, *Earth Planetary Sci. Lett.* **180**, 341–353.

Seyfried, W. E., Seewald, J. S., Berndt, M. E., Ding, K. and Foustoukos, D. I.: 2003, Chemistry of hydrothermal vent fluids from the main endavour field, northern juan de Fuca Ridge: geochemical controls in the aftermath of June 1999 seismic events, *J. Geophys. Res.* **108**, 2429.

Shewchuk, J. R.: 2002, Delaunay refinement algorithms for triangular mesh generation, *Comput. Geom. Theory Appl.* **22**, 21–74.

Shmulovich, K. I., Yardley, B. W. D. and Gonchar, G. G.: 1995, *Fluids in the Crust: Equilibrium and Transport Properties*, Chapman and Hall, London.

Sourirajan, S. and Kennedy, G. C.: 1962, The system H_2O–NaCl at elevated temperatures and pressures, *Amer. J. Sci.* **260**, 115–141.

Steefel, C. I. and MacQuarrie, K. T. B.: 1996, Approaches to modeling of reactive transport in porous media, in: P. C. Lichtner, C. I. Steefel, and E. H. Oelkers, (eds), *Reactive Transport in Porous Media, Reviews In Mineralogy* **34**, pp. 131–182.

Strang, G.: 1968, On construction and comparison of difference schemes, *SIAM J. Numer. Anal.* **5**, 506–517.

Strauss, J. M. and Schubert, G. M.: 1977, Thermal convection of water in a porous medium: Effects of temperature- and pressure-dependent thermodynamic transport properties, *J. Geophys. Res.* **82**, 3411–3421.

Stüben, K.: 2002, *User's Manual SAMG Release 21b1, July 2002*, Fraunhofer Institute SCAI, St. Augustin, Germany.

Sweby, P. K.: 1984, High resolution schemes using flux limiters for hyperbolic conservation laws, *SIAM J. Numer. Anal.* **21**, 995–1011.

Trangenstein, J. A. and Bell, J. B.: 1989a, Mathematical structure of the black-oil model for petroleum reservoir simulation, *SIAM J. Appl. Math.* **49**, 749–783.

Trangenstein, J. A. and Bell, J. B.: 1989b, Mathematical structure of compositional reservoir simulation, *SIAM J. Sci. Stat. Comput.* **10**, 817–845.

Trommsdorff, V., Skippen, G. and Ulmer, P.: 1985, Halite and sylvite as solid inclusions in high-grade metamorphic rocks, *Contributions Mineral. Petrol.* **89**, 24–29.

Ulrich, T., Günther, D. and Heinrich C. A.: 2002, Evolution of a porphyry Cu-Au deposit, based on LA-ICP-MS analysis of fluid inclusions: Bajo de la Alumbrera, Argentina (v. 96, p. 1743, 2001), *Econ. Geol.* **97**, 1888–1920.

Von Damm, K. L.: 1995, Controls on the chemistry and temporal variability of seafloor hydrothermal fluids, in: S. E. Humphris, R. A. Zierenberg, L. S. Mullineaux, and R. E. Thomson (eds.), *Seafloor Hydrothermal Systems, Geophysical Monograph* **91**, 222–247.

Xu, W.: 2004, Modeling dynamic marine gas hydrate systems, *Amer. Mineral.* **89**, 1271–1279.

Young, R.: 1993, Two-phase geothermal flows with conduction and the connection with Buckley–Leverett theory, *Transport Porous Media* **12**, 261–278.

Zienkiewicz, O. C. and Taylor, R. L.: 2000, *The Finite Element Method Vol. 3: Fluid Dynamics*, Butterworth-Heinemann, London.

Zyvoloski, G. A., Robinson, B. A., Dash, Z. V. and Trease, L. L.: 1996, *Users Manual for the FEHMN Application*. Los Alamos National Laboratory, LA-UR-94-3788.